

# Low Noise Heterogeneous III-V-on-Silicon-Nitride Mode-Locked Comb Laser

Stijn Cuyvers, Bahawal Haq, Camiel Op de Beeck, Stijn Poelman, Artur Hermans, Zheng Wang, Agnieszka Gocalinska, Emanuele Pelucchi, Brian Corbett, Gunther Roelkens, Kasper Van Gasse, and Bart Kuyken\*

Generating optical combs in a small form factor is of utmost importance for a wide range of applications such as datacom, LIDAR, and spectroscopy. Electrically powered mode-locked diode lasers provide combs with a high conversion efficiency, while simultaneously allowing for a dense spectrum of lines. In recent years, a number of integrated chip scale mode-locked lasers have been demonstrated. However, thus far these devices suffer from significant linear and nonlinear losses in the passive cavity, limiting the attainable cavity size and noise performance, eventually inhibiting their application scope. Here, we leverage the ultra-low losses of silicon-nitride waveguides to demonstrate a heterogeneously integrated III-V-on-silicon-nitride passively mode-locked laser with a narrow 755 MHz line spacing, a radio frequency linewidth of 1 Hz and an optical linewidth below 200 kHz. Moreover, these comb sources are fabricated with wafer scale technology, hence enabling low-cost and high volume manufacturable devices.

## 1. Introduction

Mode-locked lasers are a class of lasers that can generate ultra-short optical pulses by phase-locking a large number of lasing modes inside their cavity. These devices have played an essential role in several scientific breakthroughs such as the development of optical frequency combs and optical clocks.<sup>[1]</sup> With the advent of mode-locked fiber lasers in the past decade, mode-locked laser systems capable of generating fully stabilized optical frequency combs have become commercially available.<sup>[2]</sup> However, for applications outside a lab environment, these traditional systems are mostly too bulky, limiting their widespread use. As a result, significant effort has gone into realizing more compact and cost-efficient

comb generators, ideally integrated on a photonic chip.<sup>[3,4]</sup> This miniaturization has allowed for the identification of many new applications such as ultra-low-noise microwave signal generation,<sup>[5,6]</sup> LIDAR<sup>[7]</sup> and spectroscopy.<sup>[8]</sup> In particular dual-comb spectroscopy has received considerable interest in recent years, as this technique enables a highly multiplexed measurement of broadband absorption spectra using a single detector with an unparalleled acquisition time.<sup>[8–15]</sup>

In recent years, various approaches have been pursued to realize integrated comb generators. For example, considerable progress has been made on the development of quantum cascade laser (QCL) frequency combs for operation in the mid- and far-infrared and terahertz spectral regions.<sup>[16–19]</sup> Furthermore, resonant electro-optic comb generators, which employ phase modulation in a resonator with a strong second-order nonlinearity, have gained attention, owing to the excellent stability and unique complement of frequency reconfigurability.<sup>[20]</sup> Third, a large number of Kerr-effect-based frequency comb generators have been demonstrated using different material platforms in various spectral windows.<sup>[21–28]</sup> In these devices, a comb is generated based on nonlinear four-wave mixing in an optically pumped dispersion-engineered micro-resonator.<sup>[3]</sup> The comb spacing is in this case determined by the free spectral range (FSR) of the resonator. A drawback of these comb generators is their need for an optical pump source. Furthermore, the conversion efficiency is fundamentally limited, although some improvement can be found with so-called dark-soliton Kerr combs.<sup>[29]</sup> Moreover, the

S. Cuyvers, B. Haq, C. Op de Beeck, S. Poelman, A. Hermans, Z. Wang, G. Roelkens, K. Van Gasse, B. Kuyken  
Photonics Research Group  
Department of Information Technology  
Ghent University - imec  
Technologiepark-Zwijnaarde 126, Ghent 9052, Belgium  
E-mail: Bart.Kuyken@ugent.be

S. Cuyvers, B. Haq, C. Op de Beeck, S. Poelman, A. Hermans, Z. Wang, G. Roelkens, K. Van Gasse, B. Kuyken  
Center for Nano- and Biophotonics  
Ghent University  
Technologiepark-Zwijnaarde 126, Ghent 9052, Belgium  
A. Gocalinska, E. Pelucchi, B. Corbett  
Tyndall National Institute  
University College Cork  
Lee Maltings, Cork T12 R5CP, Ireland

 The ORCID identification number(s) for the author(s) of this article can be found under <https://doi.org/10.1002/lpor.202000485>

© 2021 The Authors. Laser & Photonics Reviews published by Wiley-VCH GmbH. This is an open access article under the terms of the Creative Commons Attribution-NonCommercial-NoDerivs License, which permits use and distribution in any medium, provided the original work is properly cited, the use is non-commercial and no modifications or adaptations are made.

DOI: 10.1002/lpor.202000485

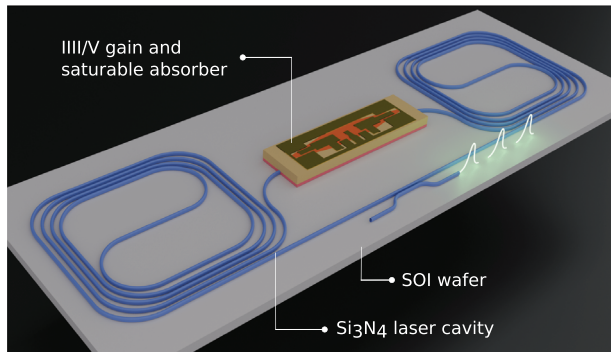


**Figure 1.** Mode-locked laser design. Artistic rendering of the extended ring cavity MLL with two 10 cm long  $\text{Si}_3\text{N}_4$  spirals and InP/InAlGaAs-based amplifiers with saturable absorber.

repetition rate of these combs as well as the other comb generator techniques tends to be beyond 10 GHz, making them ill-suited for certain applications such as high resolution spectroscopy. Recent attempts were aimed at densifying the comb spectrum of Kerr- and electro-optic-comb generators.<sup>[30,31]</sup> However, their implementations are rather complex and their comb-line spacing exceeded 2 GHz, even after densification. Mode-locked lasers on the other hand can provide low repetition rates, high conversion efficiencies, turnkey operation and are electrically powered. However, due to the high linear and nonlinear waveguide losses of the III-V platforms and the challenges associated with heterogeneous integration, current state-of-the-art integrated passively mode-locked lasers fail to demonstrate repetition rates in the sub-GHz regime.<sup>[4,14,32–39]</sup> In addition, the high waveguide losses have led to poor noise performance, inhibiting their use in various applications. Finally, state-of-the-art III-V-on-silicon MLLs provide exceptional performance but still suffer from two-photon absorption in the silicon waveguide, fundamentally limiting the attainable waveguide losses and lasing power. Therefore, transitioning from III-V-on-silicon to III-V-on-silicon-nitride eliminates these limitations and allows for a new generation of improved on-chip MLLs.

In this work, we design and demonstrate for the first time a III-V-on-silicon-nitride MLL with a sub-GHz comb line spacing of 755 MHz. Moreover, we demonstrate that this laser can generate a comb with the lowest noise performance reported to date for an on-chip mode-locked laser, such as an optical linewidth below 200 KHz and an amplified spontaneous emission (ASE) limited radio frequency (RF) linewidth of 1 Hz, paving the way for a large class of (coherent) comb applications such as LIDAR, coherent telecommunication and high-resolution spectroscopy. An illustration of the laser is shown in **Figure 1**. The combination of narrow-line spacing and low-noise performance is achieved by combining an InP/InAlGaAs-based multiple-quantum-well (MQW) semiconductor optical amplifier (SOA) with ultra-low-loss ( $5 \text{ dB m}^{-1}$ ) silicon-nitride waveguides. Thanks to recent advances in photonic technology we can now use the same material platform used to realize Kerr-based microcombs to fabricate on-chip mode-locked lasers without the need for a pump laser. Furthermore, the device is fabricated using wafer scale fabrication techniques and does not need any active alignment for the heterogeneous integration in contrast to previously demonstrated diode-pumped Kerr-combs.

## 2. Device Design and Fabrication

The laser is designed based on a ring-type extended cavity topology where a waveguide-based directional coupler is used to couple light out of the laser cavity.<sup>[4]</sup> This is a colliding-pulse mode-locked laser topology where two counter propagating pulses collide in the saturable absorber.<sup>[34,40]</sup> A rendering of the ring-cavity MLL is shown in **Figure 1**. Compared to other semiconductor MLL topologies such as Fabry–Perot-cavity MLLs, the ring-cavity MLL has the advantage that no gratings are needed, avoiding any unwanted spectral shaping. The extended ring-cavity MLL is realized using two 10 cm long and  $2 \mu\text{m}$  wide waveguide spirals that are patterned with DUV lithography in a  $\text{Si}_3\text{N}_4$  layer. The loss of the spirals is estimated to be  $0.05 \text{ dB cm}^{-1}$  at a wavelength of 1550 nm. The 330 nm thick nitride layer is deposited by means of low-pressure chemical vapor deposition (LPCVD) on top of a high quality silicon-on-insulator (SOI) wafer, which consists of a 400 nm thick silicon layer on top of a  $3 \mu\text{m}$  thermally grown silicon oxide (TOX) layer.<sup>[41]</sup> A chemical–mechanical polishing (CMP) step was employed to planarize the SOI surface prior to the silicon nitride deposition. Furthermore, as the silicon nitride thickness is only 330 nm, the waveguides exhibit  $-444 \text{ ps nm}^{-1} \text{ km}^{-1}$  normal dispersion. Utilizing thick silicon nitride waveguides with anomalous dispersion could be an attractive route to acquire shorter pulses or to explore on-chip soliton mode-locking.

A two-stage taper is employed to couple the light from the  $\text{Si}_3\text{N}_4$  waveguide to the III-V amplifier waveguide.<sup>[42,43]</sup> The light is first coupled from the nitride layer to the 400 nm thick silicon layer underneath and subsequently to the III-V layer, allowing for a better match in refractive index and consequently a higher coupling efficiency (see Experimental Section). A schematic of the two-stage taper is depicted in **Figure 2a** and an optical microscope image is shown in **Figure 2b**. Using a silicon-nitride-on-silicon-on-insulator platform has some advantages compared to the previously demonstrated amorphous-silicon-on-silicon-nitride strategy.<sup>[42]</sup> The first advantage are the reduced waveguide losses ( $0.7 \text{ dB cm}^{-1}$  versus  $20 \text{ dB cm}^{-1}$  for amorphous silicon waveguides respectively). A second drawback of using amorphous silicon is that it needs to be deposited and patterned after the silicon nitride and oxide top cladding have been fabricated. The definition of narrow amorphous silicon tapers in a recess has proven challenging, hence using a silicon-nitride-on-SOI platform allows for a higher yield with wafer-scale CMOS compatible processing.

To enable the heterogeneous integration of a III-V SOA and coupling to the silicon layer, a recess of  $1450 \mu\text{m} \times 300 \mu\text{m}$  is locally etched in the top oxide cladding using dry etching techniques, resulting in a local exposure of the silicon waveguides. Details on the SOA material composition and design can be found in the Experimental Section.

For the heterogeneous integration of the III-V amplifier in the recess on the  $\text{Si}_3\text{N}_4$  target chip, the microtransfer printing technique is used. It is based on the kinetically controlled adhesion of an elastomeric polydimethylsiloxane (PDMS) stamp to pick devices from their native substrate and print them on a target photonic integrated circuit (PIC).<sup>[42,44–47]</sup> Unlike bonding techniques, this approach allows for the integration of III/V devices in a cavity. This first demonstration of microtransfer printing in

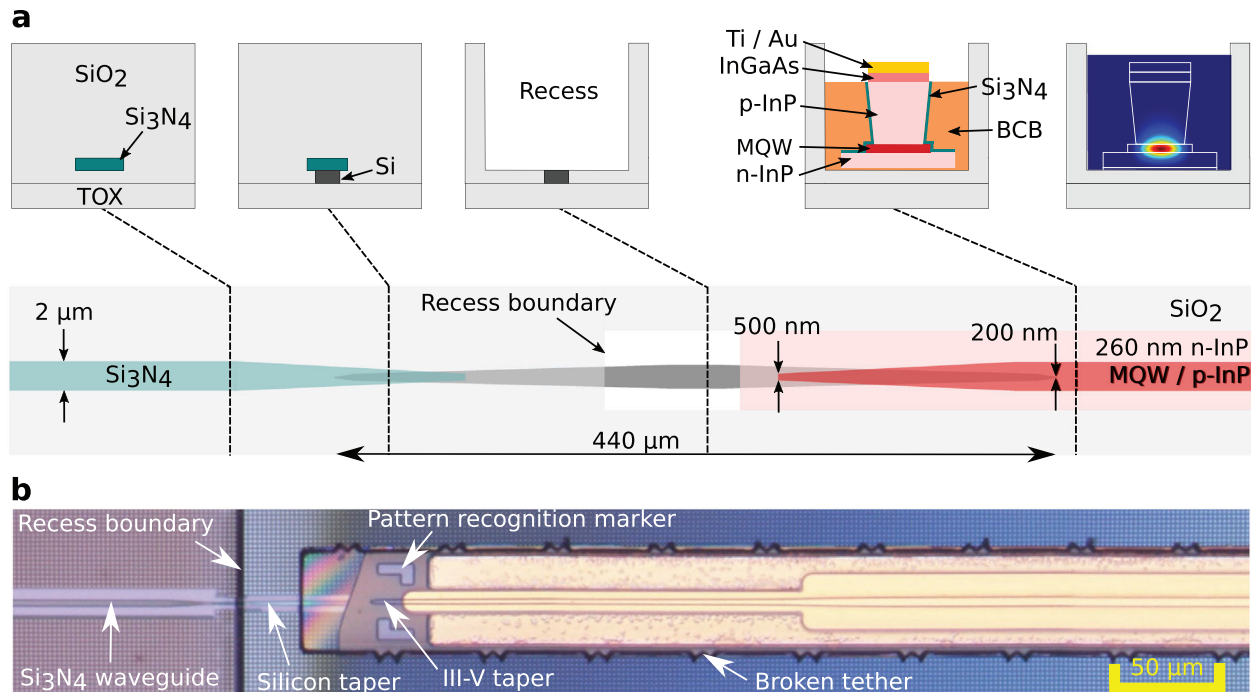


**Figure 2.** Silicon-nitride to InP/InAlGaAs waveguide taper. a) Schematic of the two-stage taper from the Si<sub>3</sub>N<sub>4</sub> to the InP/InAlGaAs amplifier through an intermediate silicon coupling layer. A cross-section is visualized for different stages of the taper and the mode profile is visualized in the III-V SOA. b) An optical microscope image of the microtransfer printed amplifier coupon on top of the taper structure.

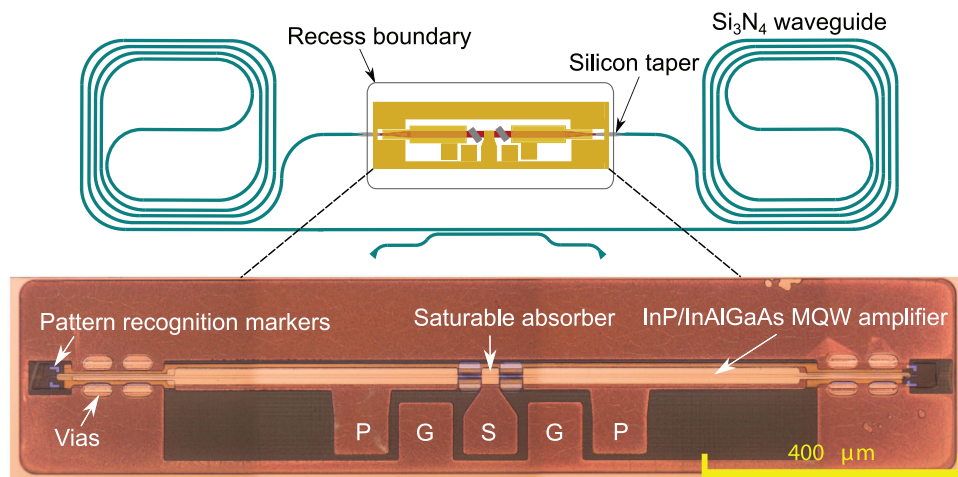


**Figure 3.** Microscope image of the InP/InAlGaAs waveguide. Optical microscope image of the post-processed coupon with saturable absorber and 600 μm long III-V amplifiers at each side. P-G-S-G-P denotes the power-signal-ground-signal-power probing pads for biasing.

a recess is a technical milestone for compatibility with ultra-low-loss top-cladded waveguide platforms. The microtransfer printing process starts by the definition of the III-V opto-electronic devices, which are denoted as "coupons", on a III-V source substrate. Next, the active devices are transferred to a target sample, which in this case is the Si<sub>3</sub>N<sub>4</sub> passive cavity chip (see Experimental Section). Finally, the active devices are post-processed to isolate the saturable absorber (SA), to open the N- and P-contacts and to add electrical contacts (see Experimental Section). A detailed description of the fabrication process is provided in Note S1, Supporting Information. An optical microscope image of the

post-processed III-V coupon is shown in **Figure 3** and the vias and probing pads are indicated. The SA is  $\approx 34 \mu\text{m}$  long and isolated by two isolation trenches of  $\approx 30 \mu\text{m}$  each. The amplifiers are 600 μm long at both sides. The footprint of the realized device is 4.7 mm<sup>2</sup>.

### 3. Device Characterization

To characterize the MLL, the chip containing the MLL was placed on a temperature-controlled chuck, which was kept at a constant temperature of 15 °C. The laser was electrically

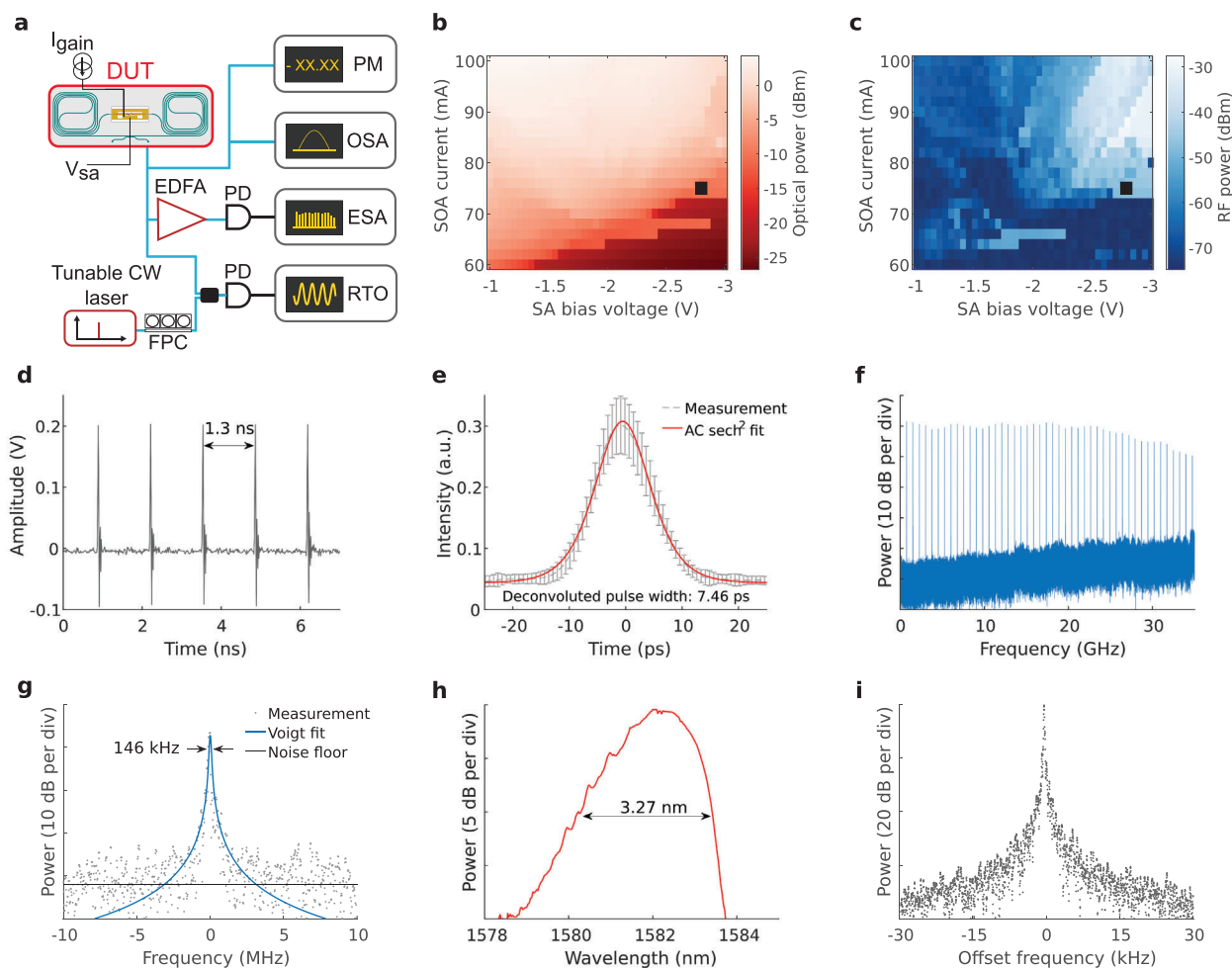


**Figure 4.** Experimental setup and results. a) Measurement setup. EDFA: erbium doped fiber amplifier; FPC: fiber polarization controller; PD: photodetector; CW: continuous wave laser; OSA: optical spectrum analyzer; PM: power meter; ESA: electrical spectrum analyzer; RTO: real-time oscilloscope. Map of the b) optical output power and c) RF power as a function of SA reverse bias voltage and SOA injection current. d–i) The operating point used to obtain results is indicated with a black square. d) Recorded pulse train by a real-time oscilloscope. e) Measured autocorrelation (AC) trace with a  $\text{sech}^2$  fit. The deconvoluted MLL pulse has a full width at half maximum (FWHM) of 7.46 ps. f) RF spectrum of the generated pulse train at the chosen operating point for a RBW of 300 kHz. g) Optical linewidth measurement by heterodyning the MLL with a Santec-770 tunable laser (RBW is 100 kHz). The black horizontal line indicates the  $-142 \text{ dBm Hz}^{-1}$  noise floor of the ESA. h) Optical spectrum, with a 10-dB span of 3.27 nm, measured with a 30 pm resolution. i) Zoom-in of the repetition frequency signal with a center frequency of 755.2 MHz (RBW is 100 Hz).

contacted using a custom-designed RF-probe, while the optical output was collected using a chip-to-fiber grating coupler and a cleaved SMF-28 fiber. A schematic overview of the measurement set-up is shown in Figure 4a. As shown in Figure 1, the MLL has a symmetric ring-cavity design resulting in two outputs. All presented measurement results were obtained from the same output. Furthermore, the measurement results were checked with the other output and were found to show no discernible difference, confirming stable operation of the symmetric ring-cavity MLL. In Figure 4b a 2D map is shown of the optical output power of the MLL, as a function of the SA bias voltage and SOA injection current. To determine which combinations of SA bias and SOA current lead to mode-locking, the electrical signal at the repetition frequency was analyzed for a wide range of settings. This was achieved by sending the optical pulse train to a

photo-receiver and analyzing the output signal with an electrical spectrum analyzer (ESA) in a band of 200 MHz centered around the designed repetition frequency of 750 MHz. In Figure 4c a map of the power of the repetition frequency signal is shown for different SA bias and SOA current settings. From this map, one can deduce that mode-locking occurs for a wide range of settings when the SOA current exceeds 70 mA and the SA bias is more negative than  $-2.0 \text{ V}$ . For a SOA current of 75 mA and a bias of  $-2.9 \text{ V}$  applied to the SA, optimal low-noise operation was identified. For these settings both the optical linewidth of the comb lines and the RF linewidth of the repetition rate were minimized.

For optimal low-noise operation the output power in the silicon-nitride waveguide is  $\approx 125 \mu\text{W}$  for a single optical output. This optical power is sufficient if the laser is to be used, for example, in an on-chip dual-comb spectrometer. It has been

demonstrated that gas-phase molecular dual-comb spectroscopy can be performed with an on-chip mode-locked laser with  $10\ \mu\text{W}$  of optical output power.<sup>[48]</sup> If for other applications higher optical output power is desired, either the amplifier inside the laser cavity can be redesigned to exhibit a lower mode confinement in the quantum wells, or an on-chip amplifier can be integrated at the output of the MLL. For example, integrated InP/InGaAsP-on-silicon optical amplifiers with an on-chip optical-output power exceeding  $50\ \text{mW}$  have been demonstrated.<sup>[49,50]</sup> Furthermore, passively mode-locked SCOWs (slab-coupled optical waveguide lasers) have been demonstrated with pulse energies beyond  $50\ \text{pJ}$ .<sup>[51]</sup> Such high-power SCOW amplifiers could in principle also be integrated through microtransfer printing. Moreover, connecting a heatsink to the amplifier or utilizing thermal shunts could improve the thermal impedance, enabling higher injection currents and therefore enhanced gain. Finally, the n-contact layer area can be enlarged to serve as a heat spreader, an approach previously demonstrated with die-to-wafer bonded devices.<sup>[14]</sup>

Figure 4d shows the pulse train of the MLL recorded using the aforementioned photo-receiver and a real-time oscilloscope (RTO). A pulse train without satellite pulses was found, confirming stable mode-locked operation. The ripple in the tail of the pulses is due to the overshoot of the photo-receiver and is an artefact not related to the optical pulse. As the analog bandwidth of both the photo-receiver and the RTO are insufficient to estimate the pulse duration, an intensity auto-correlation measurement was performed. The resulting auto-correlation trace together with a  $\text{sech}^2$  fit and the calculated deconvoluted pulse width, are shown in Figure 4e. The calculated deconvoluted pulse has a full width at half maximum (FWHM) of  $7.5\ \text{ps}$ , indicating that the generated pulses are not transform-limited. Figure 4f shows a large bandwidth ( $10\ \text{MHz}$  to  $35\ \text{GHz}$ ) electrical spectrum of the MLL at the chosen bias point. The resulting spectrum shows a flat densely-spaced RF comb spectrum with a  $755\ \text{MHz}$  line-spacing. Moreover, a high signal-to-noise ratio, exceeding  $40\ \text{dB}$ , of the repetition frequency signal and harmonics is obtained with a resolution bandwidth (RBW) of  $300\ \text{kHz}$ . This confirms stable mode-locking and strong phase coherence between the different optical modes.<sup>[52]</sup> The roll-off of the RF comb at higher frequencies is caused by the limited ( $30\ \text{GHz}$ ) analog bandwidth of the transimpedance amplifier (TIA) inside the photo-receiver. The measured repetition rate of  $755.2\ \text{MHz}$  is the lowest reported to date for any on-chip passively mode-locked laser and enables an unparalleled resolution for spectroscopy applications when compared to other on-chip approaches.<sup>[28,30,31]</sup>

For most applications the optical linewidth of the individual lasing modes is an important quality for an optical frequency comb. As the presented device primarily targets heterodyne dual-comb spectroscopy, a heterodyne measurement is most appropriate to characterize the optical linewidth. Therefore, the optical linewidth of the central lasing mode was measured by heterodyning the output of the MLL with a narrow-linewidth ( $60\ \text{kHz}$ ) external-cavity tunable laser on a photodetector. The optical linewidth of the other modes can then be extrapolated based on the knowledge of the optical linewidth of the central lasing mode and RF linewidth of the repetition frequency.<sup>[53]</sup> The beating signal of the MLL and the tunable laser was recorded using an ESA and the resulting spectrum is shown in Figure 4g.

The heterodyne signal was fitted using a Voigt profile with a FWHM of  $146\ \text{kHz}$ , based on the datapoints above the  $-142\ \text{dBm Hz}^{-1}$  noise floor of the ESA. This sub- $200\ \text{kHz}$  optical linewidth is the narrowest reported for an on-chip MLL to this date and confirms the exceptional low-noise performance of the MLL. Furthermore, the optical linewidth of the MLL approaches that of a diode-laser-pumped Kerr-comb.<sup>[54]</sup> Moreover, because of the relatively small thermo-optic coefficient of silicon nitride, the temperature sensitivity of the MLL is limited compared to devices with silicon waveguide cavities. The measured temperature sensitivity of the central lasing mode is similar to that of a state-of-the-art III-V-on-silicon-nitride CW laser (see Note S2, Supporting Information)<sup>[43]</sup>.

To determine the spectral shape of the comb, the optical spectrum of the MLL was measured with an OSA with a resolution of  $30\ \text{pm}$ , and the resulting spectrum is shown in Figure 4h. The spectral shape results from the complex interplay of the gain spectrum, absorption spectrum and the waveguide cavity properties. Asymmetric spectra are not unusual for semiconductor mode-locked lasers.<sup>[55,56]</sup> For example, the work in ref. [56] demonstrated that the mode-locked laser spectrum can be slightly skewed because the gain and absorption do not have flat spectra. The comb has a  $10\ \text{dB}$  bandwidth of  $3.27\ \text{nm}$ , corresponding with  $519$  narrowly spaced comb lines. The ability to generate several hundreds of lines with a sub-GHz linespacing and a flat-top shape is unrivaled by other comb generators such as QCLs, soliton microcombs or nanophotonic resonant EO-combs. Moreover, it allows for a flat spectrum without an intense central optical pump signal. Further engineering of the cavity, including dispersion engineering, would allow for broadening of the comb through spectral shaping of the gain. Moreover, quantum-well mode-locked lasers generating combs with a spectral bandwidth as wide as  $40\ \text{nm}$  have been demonstrated.<sup>[33,57]</sup> Finally, several of these MLLs can be integrated and multiplexed on a single chip allowing to span any wavelength interval of interest. Such a superposition approach can consist of various sub-combs that are mutually incoherent as, for example, dual-comb spectroscopy can be carried out for each spectral region separately.<sup>[12]</sup> Currently the optical comb is too narrow to directly measure the carrier-envelope offset frequency. However, in future work one could use on-chip amplification of the output pulse and on-chip nonlinear broadening to achieve a wider comb.

The repetition frequency RF linewidth is a commonly used figure of merit for the noise properties of a semiconductor mode-locked laser.<sup>[4,39]</sup> Furthermore, the RF linewidth is related to both the timing-jitter of the pulse train, the comb-line spacing noise and the optical linewidth of the comb lines.<sup>[52,53]</sup> A  $60\ \text{kHz}$  wide ESA spectrum, centered at the repetition frequency, measured with a  $100\ \text{Hz}$  resolution bandwidth (RBW) and a  $25\ \text{Hz}$  frequency spacing is depicted in Figure 4i. From the graph it is clear that the repetition rate has a high signal-to-noise ratio (SNR) and a very small FWHM. Due to the narrow RF linewidth, a quantitative analysis can only reliably be achieved using a single-sideband phase-noise (SSB-PN) measurement, as discussed in Section 4. From Figure 4i, a qualitative  $-10\ \text{dB}$  RF linewidth of  $300\ \text{Hz}$  can be deduced from the raw data. The narrow RF linewidth indicates that all optical modes are tightly phase-locked and that the optical linewidth of all comb lines is similar to the linewidth of the central lasing mode.<sup>[53]</sup> However, the RF linewidth deviates

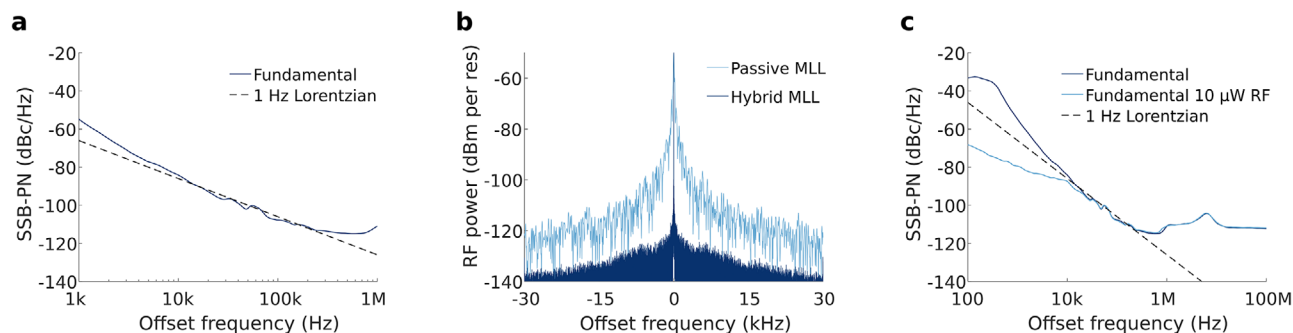


**Figure 5.** Single-sideband phase-noise measurement results. a) Single-sideband phase noise (SSB-PN) of the repetition-frequency beat signal. A fundamental RF linewidth of 1 Hz FWHM is achieved. b) Impact of hybrid mode-locking on the RF linewidth of the fundamental 755.2 MHz tone. c) SSB-PN for hybrid mode-locking. Hybrid operation suppresses the low frequency noise but leaves the Lorentzian noise undisturbed.

from the expected Lorentzian profile and is therefore broadened by noise not related to laser dynamics. To gain additional insight in the noise sources affecting the laser, a single-sideband phase-noise (SSB-PN) measurement of the repetition frequency is performed.

#### 4. Single Sideband Phase Noise Measurement

For passively mode-locked semiconductor lasers, the RF linewidth of the repetition frequency signal is in most cases dominated by the ASE-induced timing jitter of the pulse train.<sup>[52,58–62]</sup> In this case the repetition frequency signal has a Lorentzian profile. However, if the Lorentzian linewidth becomes sufficiently narrow the RF linewidth can be dominated by environmental and technical noise resulting in a non-Lorentzian profile.<sup>[39]</sup> To determine the RF linewidth achievable when eliminating technical and environmental noise, a SSB-PN measurement can be performed.<sup>[59]</sup> **Figure 5a** shows the SSB-PN of the repetition frequency signal (755 MHz) at sufficiently large offset frequencies from the carrier to avoid influence of technical noise. Together with the measured SSB-PN, a Lorentzian profile with a 1 Hz FWHM is plotted. It is clear that between 10 and 200 kHz the SSB-PN follows the Lorentzian profile, while at lower frequencies the influence of technical noise becomes apparent. This can be attributed to acoustic noise sources, which result from both air circulation as well as vibrations from the lab environment. As the presented device has not been packaged and is hence not shielded in any way from acoustic perturbations, the technical noise is significant. Moreover, the device was characterized using contact probes, cleaved fibers (not glued) for coupling, as well as long optical fiber cables, making the experimental setup susceptible to acoustic disturbances. For commercial deployment, the device could be packaged using a butterfly package, glued fibers and wire bonded contacts, greatly limiting the device's susceptibility to acoustic perturbations. However, environmental temperature changes could still affect the stability of the mode-locked laser. If a fully stabilized optical comb is desired, it will be necessary to include feedback circuitry with thermoelectric actuators, enabling continuous stabilization of the laser cavity.

At offset frequencies exceeding 200 kHz the white noise floor of the photo-receiver is reached. To verify the Lorentzian profile of the RF linewidth, the SSB-PN of several harmonics of

the repetition frequency were measured and analyzed (see Note S2, Supporting Information). The resulting ASE-limited 1 Hz RF linewidth is the lowest reported so far and is determined in the same way as was done for the previously reported narrowest linewidths.<sup>[59]</sup> This 1 Hz linewidth corresponds to a pulse-to-pulse root-mean-square timing jitter of 19 fs for a repetition period of 1.3 ns.<sup>[60]</sup> Furthermore from the SSB-PN, a timing jitter power spectral density (PSD) of  $111 \text{ fs}^2 \text{ Hz}^{-1}$  at a 10 kHz offset frequency and an integrated timing jitter of 1 ps for a frequency range between 10 kHz and 1 MHz are calculated (see Note S3, Supporting Information). Low-noise fiber lasers on the other hand routinely achieve timing jitter PSDs around  $10^{-3} \text{ fs}^2 \text{ Hz}^{-1}$  and integrated timing jitters below 20 fs.<sup>[63]</sup> This performance gap can be attributed to several factors and a more elaborate comparison with solid-state and fiber mode-locked lasers is provided in Note S3, Supporting Information.

Although the laser shows excellent stability and noise performance, for a number of applications it is useful if the line-spacing can be locked to an external RF synthesizer, as this allows for relating the comb-line spacing to a frequency standard such as a hydrogen maser. To lock the comb-line spacing one can modulate the saturable absorber with the output of a reference frequency synthesizer, effectively gating the optical pulse train.<sup>[60]</sup> To experimentally lock the MLL to a synthesizer hybrid mode-locking is employed, where the SA is modulated with the low-power (10  $\mu\text{W}$ ) output of a low-noise synthesizer at the repetition frequency of the passively MLL. The spectrum centered on the repetition frequency for both passive and hybrid mode-locking is shown in **Figure 5b**. Under hybrid mode-locking, a clear single frequency signal with high SNR exactly matching the driving signal frequency is found. This confirms that the repetition rate is locked to the synthesizer. For low RF powers we find a locking range of  $\approx 10$  kHz. The SSB-PN measured under both passive and hybrid mode-locking is shown in **Figure 5c**. It is clear that for frequencies below 10 kHz the phase noise is strongly suppressed by locking the laser to the reference synthesizer. For higher frequencies the phase-noise remains unchanged and is dominated by the ASE-induced pulse train timing jitter. At the same time the noise floor at higher offset frequencies is still dominated by the amplitude noise coming from the TIA. These results show that the line-spacing can be locked to a synthesizer with a low-power RF signal of 10  $\mu\text{W}$  (22 mV), hereby offering

a straightforward solution to eliminate any residual line-spacing noise.

## 5. Conclusion

To conclude, we have successfully demonstrated a III-V-on-silicon-nitride passively mode-locked laser on a photonic chip with a record-low repetition rate of 755 MHz. By using a long low-loss extended  $\text{Si}_3\text{N}_4$  ring cavity, unparalleled noise performance is achieved with a narrow optical linewidth below 200 kHz and an ASE-limited RF linewidth of 1 Hz. These record values indicate that this MLL is the lowest noise on-chip passively MLL presented in literature to date, and illustrates the superior noise performance a III-V-on-silicon-nitride-on-silicon-on-insulator platform can offer compared to conventional monolithic III-V, InP, and III-V-on-Si platforms. The device was fabricated by means of microtransfer printing an InP/InAlGaAs-based multiple quantum-well coupon in a recess, enabling wafer scale manufacturing. State-of-the-art microtransfer printers can support high throughput integration by utilizing array stamps, enabling multiple coupons to be picked up and printed simultaneously. Moreover, pattern recognition can be used to automatically align the intended picking and printing locations on the source and target wafer.

Such an integrated and electrically pumped dense comb generator provides several advantages in terms of cost, device foot-print, robustness, and power consumption, enabling its use in high-resolution spectroscopic applications. Furthermore, the presented work can be extended to target various other applications such as datacom, telecom, and low-noise microwave signal generation by changing the comb line spacing while at the same time keeping the excellent noise properties. This can for example be achieved by introducing a high-finesse resonator filter inside the laser cavity<sup>[64,65]</sup> or by co-integrating a pulse interleaver.<sup>[66]</sup>

## 6. Experimental Section

**Two-Stage Taper Design:** To couple the light from the  $\text{Si}_3\text{N}_4$  waveguide to the AlGaInAs gain waveguide, a custom taper structure was designed using an intermediate crystalline silicon waveguide. The taper structure as well as some cross-sections at various locations along the taper are indicated in Figure 2a. The  $\text{Si}_3\text{N}_4$  waveguide was tapered over a length of 155  $\mu\text{m}$  and was terminated at a distance of 10  $\mu\text{m}$  from the recess boundary. The silicon waveguide had a total length of 440  $\mu\text{m}$ , and consisted of a 160  $\mu\text{m}$  and a 180  $\mu\text{m}$  taper, respectively at the  $\text{Si}_3\text{N}_4$  and the III-V side. In between the two silicon tapers was a 2  $\mu\text{m}$  wide silicon waveguide with a length of 100  $\mu\text{m}$ . The recess in the top cladding starts and ends at a distance of 110  $\mu\text{m}$  from the Si taper tips. This ensured that the mode was well confined to the silicon waveguide at the recess interfaces, minimizing parasitic reflections. The MQW layers and p-InP was tapered to a tip width of 500 nm at a distance of 150  $\mu\text{m}$  from the recess interfaces to couple the light from the silicon to the III-V and vice versa. The III-V tapers were based on the alignment tolerant design, proposed in ref. [46].

**III/V Layer Stack:** The III/V SOA layer stack consisted of a 200 nm n-doped InP cathode on top of a 60 nm intrinsic InP layer, six InAlGaAs quantum wells and barriers, a 25 nm etch stop InGaAsP layer underneath a 1.5  $\mu\text{m}$  p-doped InP cladding and a 200 nm highly p-doped InGaAs contact layer. The quantum wells and barriers were surrounded by a pair of 75 nm thick InAlGaAs separate confinement heterostructure (SCH) layers and a

pair of 40 nm thick InAlGaAs transition layers. More details can be found in ref. [46], where an identical layer stack was employed.

**Microtransfer Printing Process:** A thin adhesive layer of a BCB:mesitylene 1:4 solution was spincoated on the  $\text{Si}_3\text{N}_4$  target chip at 3000 rpm for 40 s and baked at 150 °C for 10 min. This adhesive layer was  $\approx 50$  nm thin (before printing), and enhanced the yield of the microtransfer printing process. Moreover it effectively planarized surface roughness in the recess. After baking, the sample was cooled down at a slow pace, without the use of a heatsink, to avoid the formation of bubbles in the deposited layer. The III-V coupons were transfer printed using the X-Celeprint  $\mu\text{TP}$ -100 microtransfer printing tool with a 1400  $\mu\text{m} \times 50$   $\mu\text{m}$  PDMS stamp. An alignment accuracy of 1  $\mu\text{m}$  ( $3\sigma$ ) was achieved for printing single coupons. In case high-throughput wafer-scale fabrication was envisioned, one could utilize so-called array stamps enabling multiple coupons to be picked up and printed simultaneously. Commercial microtransfer printing tools provided an alignment accuracy of 1.5  $\mu\text{m}$  ( $3\sigma$ ) for large array printing.<sup>[42]</sup>

**Post-Processing:** After transfer printing, the encapsulation was removed with an oxygen plasma and the adhesive BCB layer was cured at 180 °C. Thereafter, a BCB cladding was spincoated for 40 s at 2000 rpm and cured at 280 °C. The BCB was subsequently etched back by means of dry etching to expose the top of the mesa. As the printed coupon was a conventional SOA, a saturable absorber still needed to be defined to enable mode-locking. For this purpose, two isolation trenches were defined with a width of 30  $\mu\text{m}$  and separated by 34  $\mu\text{m}$ . The Au and Ti metal of the anode were locally removed by means of a  $\text{KI}/\text{I}_2$  and a 1% buffered HF wet etch, respectively. Afterward, an inductively coupled plasma (ICP) etch at 60 °C with  $\text{CH}_4$  and  $\text{H}_2$  gasses was used to locally remove the In-GaAs. A photoresist mask with 45° inclined trenches was used for the ICP etch to suppress parasitic reflections from the discontinuity of the layer stack. Next, vias were etched to access the n-InP cathode using a thick AZ10XT photoresist. By reflowing a thick resist, vias with a gradual slope were achieved, ensuring proper metal coverage. Finally, 1  $\mu\text{m}$  Au with a 40 nm Ti adhesion layer was deposited for electrical contacting.

**Measurement Setup Details:** The MLL characterization was carried out using a custom-made temperature controlled chuck consisting of an aluminium block on top of a Peltier element, which was controlled using a Thorlabs TH10K thermistor and a TED200C temperature controller. This setup allowed to keep the device substrate at a temperature of 15 °C. A simplified schematic of the measurement setup is depicted in Figure 4a. The coupling from the waveguides to single-mode optical fibers was realized by using  $\text{Si}_3\text{N}_4$  grating couplers, which exhibited a coupling loss of  $\approx 9$  dB per coupler at 1580 nm. The MLL was biased using two Keithley 2400 source meter units. The RF comb spectrum was recorded using an Agilent electrical spectrum analyzer (N9010A) with a frequency operation range of 10 Hz to 44 GHz. To measure the repetition rate frequency, the ESA was used in FFT mode with a RBW of 100 Hz and a frequency span of 200 kHz. The optical spectrum was recorded with an Anritsu MS9740A OSA with a resolution of 30 pm. The optical linewidth was measured by combining the output of a Santec-770 tunable laser (60 kHz) with the output of the MLL, using a fiber coupler, and detecting them with a Discovery photo-receiver (DSC-R409). The generated output of the photodetector was then analyzed with the ESA set to a 400 MHz span with a 100 kHz RBW. Auto-correlation measurements were carried out with an APE pulseCheck intensity autocorrelator.

## Supporting Information

Supporting Information is available from the Wiley Online Library or from the author.

## Acknowledgements

The authors acknowledge the Flemish Research Council (FWO) for Ph.D. scholarships (11F8120N and 1S54418N) and a postdoctoral fellowship (12ZB520N). This work was carried out in the context of the European

Research Council (ERC) starting grant ELECTRIC and the INTERREG-fwlv SAFESIDE project. The authors also acknowledge the support from Science Foundation Ireland under grant 12/RC/2276, 12/RC/2276-P2, and 15/IA/2864.

## Conflict of Interest

The authors declare no conflict of interest.

## Data Availability Statement

The data that support the findings of this study are available from the corresponding author upon reasonable request.

## Keywords

dual-comb spectroscopy, heterogeneous integration, mode-locked lasers, optical frequency comb, quantum well lasers, semiconductor lasers, transfer printing

Received: November 2, 2020

Revised: March 23, 2021

Published online:

- [1] S. A. Diddams, K. Vahala, T. Udem, *Science* **2020**, 369, 6501.
- [2] P. Del'Haye, O. Arcizet, M. L. Gorodetsky, R. Holzwarth, T. J. Kippenberg, *Nat. Photonics* **2009**, 3, 529.
- [3] A. L. Gaeta, M. Lipson, T. J. Kippenberg, *Nat. Photonics* **2019**, 13, 158.
- [4] K. Van Gasse, S. Uvin, V. Moskalenko, S. Latkowski, G. Roelkens, E. Bente, B. Kuyken, *IEEE Photon. Technol.* **2019**, 31, 1870.
- [5] J. Liu, E. Lucas, A. S. Raja, J. He, J. Riemensberger, R. N. Wang, M. Karpov, H. Guo, R. Bouchand, T. J. Kippenberg, *Nat. Photonics* **2020**, 14, 486.
- [6] X. Xie, R. Bouchand, D. Nicolodi, M. Giunta, W. Hänsel, M. Lezius, A. Joshi, S. Datta, C. Alexandre, M. Lours, P.-A. Tremblin, G. Santarelli, R. Holzwarth, Y. Le Coq, *Nat. Photonics* **2017**, 11, 44.
- [7] P. Trocha, M. Karpov, D. Ganin, M. H. P. Pfeiffer, A. Kordts, S. Wolf, J. Krockenberger, P. Marin-Palomo, C. Weimann, S. Randel, W. Freude, T. J. Kippenberg, C. Koos, *Science* **2018**, 359, 887.
- [8] A. Dutt, C. Joshi, X. Ji, J. Cardenas, Y. Okawachi, K. Luke, A. L. Gaeta, M. Lipson, *Sci. Adv.* **2018**, 4, 3.
- [9] N. Picqué, T. W. Hänsch, *Nat. Photonics* **2019**, 13, 146.
- [10] I. Coddington, N. Newbury, W. Swann, *Optica* **2016**, 3, 414.
- [11] M. A. Abbas, Q. Pan, J. Mandon, S. M. Cristescu, F. J. M. Harren, A. Khodabakhsh, *Sci. Rep.* **2019**, 9, 17247.
- [12] A. Shams-Ansari, M. Yu, Z. Chen, C. Reimer, M. Zhang, N. Picqué, M. Lončar, arXiv:2003.04533, **2020**.
- [13] G. Millot, S. Pitois, M. Yan, T. Hovhannisyan, A. Bendahmane, T. W. Hänsch, N. Picqué, *Nat. Photonics* **2016**, 10, 27.
- [14] Z. Wang, K. Van Gasse, V. Moskalenko, S. Latkowski, E. Bente, B. Kuyken, G. Roelkens, *Light Sci. Appl.* **2017**, 6, e16260.
- [15] D. Grassani, E. Tagkoudi, H. Guo, C. Herkommer, F. Yang, T. J. Kippenberg, C.-S. Brès, *Nat. Commun.* **2019**, 10, 1553.
- [16] L. Consolino, M. Nafa, F. Cappelli, K. Garrasi, F. P. Mezzapesa, L. Li, A. G. Davies, E. H. Linfield, M. S. Vitiello, P. De Natale, S. Bartalini, *Nat. Commun.* **2019**, 10, 2938.
- [17] B. Meng, M. Singleton, M. Shahmohammadi, F. Kapsalidis, R. Wang, M. Beck, J. Faist, *Optica* **2020**, 7, 162.
- [18] M. Piccardo, P. Chevalier, S. Anand, Y. Wang, D. Kazakov, E. A. Mejia, F. Xie, K. Lascola, A. Belyanin, F. Capasso, *Appl. Phys. Lett.* **2018**, 113, 031104.
- [19] Y. Yang, D. Burghoff, D. J. Hayton, J.-R. Gao, J. L. Reno, Q. Hu, *Optica* **2016**, 3, 499.
- [20] M. Zhang, B. Buscaino, C. Wang, A. Shams-Ansari, C. Reimer, R. Zhu, J. M. Kahn, M. Lončar, *Nature* **2019**, 568, 373.
- [21] P. Del'Haye, A. Schliesser, O. Arcizet, T. Wilken, R. Holzwarth, T. J. Kippenberg, *Nature* **2007**, 450, 1214.
- [22] A. G. Griffith, R. K. Lau, J. Cardenas, Y. Okawachi, A. Mohanty, R. Fain, Y. H. D. Lee, M. Yu, C. T. Phare, C. B. Poitras, A. L. Gaeta, M. Lipson, *Nat. Commun.* **2015**, 6, 6299.
- [23] B. Stern, X. Ji, Y. Okawachi, A. L. Gaeta, M. Lipson, *Nature* **2018**, 562, 401.
- [24] H. Jung, C. Xiong, K. Y. Fong, X. Zhang, H. X. Tang, *Opt. Lett.* **2013**, 38, 2810.
- [25] B. J. M. Hausmann, I. Bulu, V. Venkataraman, P. Deotare, M. Lončar, *Nat. Photonics* **2014**, 8, 369.
- [26] L. Razzari, D. Duchesne, M. Ferrera, R. Morandotti, S. Chu, B. E. Little, D. J. Moss, *Nat. Photonics* **2010**, 4, 41.
- [27] L. Chang, W. Xie, H. Shu, Q.-F. Yang, B. Shen, A. Boes, J. D. Peters, W. Jin, C. Xiang, S. Liu, G. Moille, S.-P. Yu, X. Wang, K. Srinivasan, S. B. Papp, K. Vahala, J. E. Bowers, *Nat. Commun.* **2020**, 11, 1331.
- [28] M.-G. Suh, K. Vahala, *Optica* **2018**, 5, 65.
- [29] A. Fülöp, M. Mazur, A. Lorences-Riesgo, Ó. B. Helgason, P.-H. Wang, Y. Xuan, D. E. Leaird, M. Qi, P. A. Andrekson, A. M. Weiner, V. TorresCompany, *Nat. Commun.* **2018**, 9, 1598.
- [30] C. Bao, Z. Yuan, H. Wang, L. Wu, B. Shen, K. Sung, S. Leifer, Q. Lin, K. Vahala, *Optica* **2020**, 7, 309.
- [31] A. Shams-Ansari, C. Reimer, N. Sinclair, M. Zhang, N. Picqué, M. Loncar, in *Conf. on Lasers and Electro-Optics*, OSA Publishing, Washington, DC **2020**.
- [32] Z. Lu, J. Liu, S. Raymond, P. Poole, P. Barrios, D. Poitras, *Opt. Express* **2008**, 16, 10835.
- [33] V. Moskalenko, S. Latkowski, S. Tahvili, T. de Vries, M. Smit, E. Bente, *Opt. Express* **2014**, 22, 28865.
- [34] S. Latkowski, V. Moskalenko, S. Tahvili, L. Augustin, M. Smit, K. Williams, E. Bente, *Opt. Lett.* **2015**, 40, 77.
- [35] V. Corral, R. Guzmán, C. Gordón, X. J. M. Leijtens, G. Carpintero, *Opt. Lett.* **2016**, 41, 1937.
- [36] J. H. Marsh, L. Hou, *IEEE J. Sel. Top. Quantum Electron.* **2017**, 23, 1.
- [37] S. Liu, X. Wu, D. Jung, J. C. Norman, M. J. Kennedy, H. K. Tsang, A. C. Gossard, J. E. Bowers, *Optica* **2019**, 6, 128.
- [38] M.-C. Lo, R. Guzmán, G. Carpintero, *Opt. Lett.* **2018**, 43, 507.
- [39] M. L. Davenport, S. Liu, J. E. Bowers, *Photon. Res.* **2018**, 6, 468.
- [40] S. Keyvaninia, S. Uvin, M. Tassaert, X. Fu, S. Latkowski, J. Mariën, L. Thomassen, F. Lelarge, G. Duan, P. Verheyen, G. Lepage, J. V. Campenhout, E. Bente, G. Roelkens, *Opt. Express* **2015**, 23, 3221.
- [41] W. D. Sacher, Y. Huang, G. Lo, J. K. S. Poon, *J. Light. Technol.* **2015**, 33, 901.
- [42] C. Op de Beeck, B. Haq, L. Elsinger, A. Gocalinska, E. Pelucchi, B. Corbett, G. Roelkens, B. Kuyken, *Optica* **2020**, 7, 386.
- [43] C. Xiang, W. Jin, J. Guo, J. D. Peters, M. J. Kennedy, J. Selvidge, P. A. Morton, J. E. Bowers, *Optica* **2020**, 7, 20.
- [44] A. De Groote, P. Cardile, A. Z. Subramanian, A. M. Fecioru, C. Bower, D. Delbeke, R. Baets, G. Roelkens, *Opt. Express* **2016**, 24, 13754.
- [45] J. Zhang, G. Muliuk, J. Juvert, S. Kumari, J. Goyvaerts, B. Haq, C. Op de Beeck, B. Kuyken, G. Morthier, D. Van Thourhout, R. Baets, G. Lepage, P. Verheyen, J. Van Campenhout, A. Gocalinska, J. O'Callaghan, E. Pelucchi, K. Thomas, B. Corbett, A. J. Trindade, G. Roelkens, *APL Photonics* **2019**, 4, 110803.
- [46] B. Haq, S. Kumari, K. Van Gasse, J. Zhang, A. Gocalinska, E. Pelucchi, B. Corbett, G. Roelkens, *Laser Photonics Rev.* **2020**, 14, 1900364.

- [47] J. Justice, C. Bower, M. Meitl, M. B. Mooney, M. A. Gubbins, B. Corbett, *Nat. Photonics* **2012**, *6*, 610.
- [48] K. Van Gasse, Z. Chen, E. Vicentini, J. Huh, S. Poelman, Z. Wang, G. Roelkens, T. W. Hänsch, B. Kuyken, N. Picqué, arXiv:2006.15113, **2020**.
- [49] K. Van Gasse, R. Wang, G. Roelkens, *Opt. Express* **2019**, *27*, 293.
- [50] M. L. Davenport, S. Skendžić, N. Volet, J. C. Hulme, M. J. R. Heck, J. E. Bowers, *IEEE J. Sel. Top. Quantum Electron.* **2016**, *22*, 78.
- [51] P. W. Juodawlkis, J. J. Plant, W. Loh, L. J. Missaggia, F. J. O'Donnell, D. C. Oakley, A. Napoleone, J. Klamkin, J. T. Gopinath, D. J. Ripin, S. Gee, P. J. Delfyett, J. P. Donnelly, *IEEE J. Sel. Top. Quantum Electron.* **2011**, *17*, 1698.
- [52] D. von der Linde, *Appl. Phys. B* **1986**, *39*, 201.
- [53] T. Habruseva, S. O'Donoghue, N. Rebrova, F. Kéfélian, S. Hegarty, G. Huyet, *Opt. Lett.* **2009**, *34*, 3307.
- [54] A. S. Raja, A. S. Voloshin, H. Guo, S. E. Agafonova, J. Liu, A. S. Gorodnitskiy, M. Karpov, N. G. Pavlov, E. Lucas, R. R. Galiev, A. E. Shitikov, J. D. Jost, M. L. Gorodetsky, T. J. Kippenberg, *Nat. Commun.* **2019**, *10*, 680.
- [55] S. Uvin, S. Keyvaninia, F. Lelarge, G.-H. Duan, B. Kuyken, G. Roelkens, *Opt. Express* **2016**, *24*, 5277.
- [56] V. Moskalenko, K. A. Williams, E. A. J. M. Bente, *IEEE Photonics J.* **2016**, *8*, 1502810.
- [57] V. Moskalenko, K. Williams, J. Koelemeij, E. Bente, in *Int. Semicond. Laser Conf.*, IEEE, Piscataway, NJ, **2016**, pp. 1–2.
- [58] F. Kefelian, S. O'Donoghue, M. T. Todaro, J. G. McInerney, G. Huyet, *IEEE Photon. Technol.* **2008**, *20*, 1405.
- [59] D. Auth, S. Liu, J. Norman, J. E. Bowers, S. Breuer, *Opt. Express* **2019**, *27*, 27256.
- [60] L. Drzewietzki, S. Breuer, W. Elsässer, *Opt. Express* **2013**, *21*, 16142.
- [61] R. Paschotta, *Appl. Phys. B* **2004**, *79*, 153.
- [62] R. Paschotta, *Appl. Phys. B* **2004**, *79*, 163.
- [63] J. Kim, Y. Song, *Adv. Opt. Photon.* **2016**, *8*, 465.
- [64] E. Chae, E. Kambe, K. Motohara, H. Izumiura, M. Doi, K. Yoshioka, arXiv:2101.05926, **2021**.
- [65] K. Bagnell, A. Klee, P. J. Delfyett, J. J. Plant, P. W. Juodawlkis, *Opt. Lett.* **2018**, *43*, 2396.
- [66] M.-C. Lo, R. Guzmán, C. Gordón, G. Carpintero, *Opt. Lett.* **2017**, *42*, 1532.